

RESEARCH ARTICLE | JUNE 03 2024

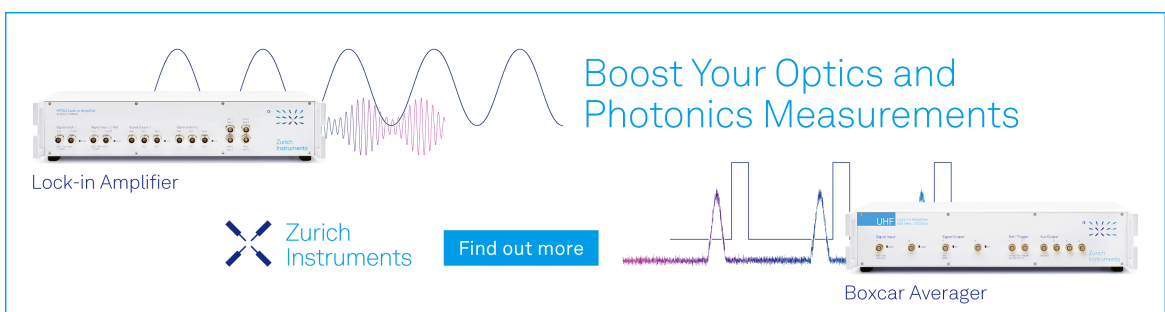
## A dynamic thermal sensing mechanism with reconfigurable expanded-plane structures

Haohan Tan; Haoyang Cai; Peng Jin  ; Jiping Huang  



J. Appl. Phys. 135, 214501 (2024)

<https://doi.org/10.1063/5.0207725>



Boost Your Optics and Photonics Measurements

Lock-in Amplifier

Zurich Instruments

Find out more

Boxcar Averager

# A dynamic thermal sensing mechanism with reconfigurable expanded-plane structures

Cite as: J. Appl. Phys. 135, 214501 (2024); doi: 10.1063/5.0207725

Submitted: 22 March 2024 · Accepted: 20 May 2024 ·

Published Online: 3 June 2024



View Online



Export Citation



CrossMark

Haohan Tan, Haoyang Cai, Peng Jin,<sup>a)</sup> and Jiping Huang<sup>b)</sup>

## AFFILIATIONS

Department of Physics, State Key Laboratory of Surface Physics and Key Laboratory of Micro and Nano Photonic Structures (MOE), Fudan University, Shanghai 200438, China

<sup>a)</sup>Electronic mail: 19110190022@fudan.edu.cn

<sup>b)</sup>Author to whom correspondence should be addressed: jphuang@fudan.edu.cn

## ABSTRACT

The precise measurement of temperature is crucial in various fields such as biology, medicine, industrial automation, energy management, and daily life applications. While in most scenarios, sensors with a fixed thermal conductivity inevitably mismatch the analogous parameter of the medium being measured, thus causing the distortion and inaccurate detection of original temperature fields. Despite recent efforts on addressing the parameter-mismatch issue, all current solutions are constrained to a fixed working medium, whereas a more universal sensor should function in a variety of scenes. Here, we report a dynamic and reconfigurable thermal sensor capable of highly accurate measurements in diverse working environments. Remarkably, thanks to the highly tunable thermal conductivity of the expanded-plane structure, this sensor works effectively on background mediums with a wide range of conductivity. Such a development greatly enhances the robustness and adaptability of thermal sensors, setting a solid foundation for applications in multi-physical sensing scenarios.

© 2024 Author(s). All article content, except where otherwise noted, is licensed under a Creative Commons Attribution (CC BY) license (<https://creativecommons.org/licenses/by/4.0/>). <https://doi.org/10.1063/5.0207725>

## I. INTRODUCTION

Over the past few decades, the field of thermal metamaterials has witnessed significant advancements.<sup>1–7</sup> Researchers have introduced an array of devices with novel functionalities, encompassing thermal cloaks,<sup>8–11</sup> concentrators,<sup>12–19</sup> rotators,<sup>20,21</sup> and sensors based on thermotaxis and scattering cancellation techniques.<sup>22–25</sup> Notably, the concept of topology has also been integrated into thermal metamaterials.<sup>26–30</sup> Among these devices, thermal sensors have garnered considerable attention due to their pivotal role in the temperature field detection. However, a prevalent shortcoming of conventional thermal sensors is their proclivity to distort the measured temperature field, resulting in inaccuracies in the obtained results. To address this issue, various solutions have been proposed.<sup>31–34</sup> For instance, Xu *et al.* introduced the concept of a thermal invisible sensor.<sup>31,33</sup> By solving the linear Laplace equation, they derived two groups of thermal conductivities to realize thermally invisible sensors, encompassing geometrically anisotropic cases. Their bilayer scheme can maintain the original temperatures in both the sensor and the background. Subsequently, considering the combination of radiation and conduction, described by

Fourier's law and Rosseland diffusion approximation, respectively, Wang *et al.* accommodated multiphysics fields<sup>32</sup> to achieve thermal sensors. Jin *et al.* also proposed an anisotropic monolayer scheme to prevent thermal sensors from distorting local and background temperature profiles, thereby ensuring accuracy and thermal invisibility.<sup>33</sup> They further introduced an optimization model utilizing particle swarm algorithms to create bilayer thermal sensors composed of bulk isotropic materials.<sup>34,35</sup> They selected suitable materials for different regions and treated the radii of the sensor, inner shell, and outer shell as design variables, ultimately minimizing the fitness function through particle swarm optimization. Their model can also be flexibly extended to the square case.

Nevertheless, despite substantial efforts to address the parameter-mismatch issue, current solutions primarily concentrate on a fixed background environment where the thermal conductivity of the background region remains constant. This raises a crucial unresolved problem: how to design a versatile and reconfigurable sensor capable of adapting to varying background environments. In this context, “reconfigurability” refers to the sensor’s ability to effectively operate amid changes in the background environment.

03 June 2024 10:32:02

Existing studies indicate that for bilayer sensors, any alteration in the thermal conductivity of the background region necessitates adjustments in the thermal conductivity of the core or shell region. In practical applications, this would entail altering the material composition of the core or shell region, which becomes impractical due to the wide range of potential background environments. Recently, an innovative type of thermal metamaterials based on an expanded-plane (EP) configuration has been proposed.<sup>36</sup> This structure not only facilitates ultrahigh effective thermal conductivity but also allows for the adjustment of effective thermal conductivity by simply modifying the height of the expanded plane, thereby offering new possibilities for the development of reconfigurable thermal sensors [refer to Figs. 1(a)–1(d)]. Building upon the EP structure,

Han *et al.* have also designed a thermal cloak using a single material, thus eliminating interfacial thermal resistance.<sup>10,37–40</sup>

In this paper, we present the design of a single expanded-plane (SEP) bilayer sensor and evaluate its performance through both simulations and experiments. Among various numerical methods,<sup>41–44</sup> we opt for the finite-element simulation method due to its distinct advantages. The results unequivocally affirm that by simply adjusting the height of the expanded plane, the SEP sensor can efficiently operate in a diverse range of environments, thereby demonstrating its reconfigurability. Furthermore, similar outcomes are obtained when employing multiple expanded-plane (MEP) structures.

In comparison to the existing research, our design demonstrates adaptability to environments characterized by varying

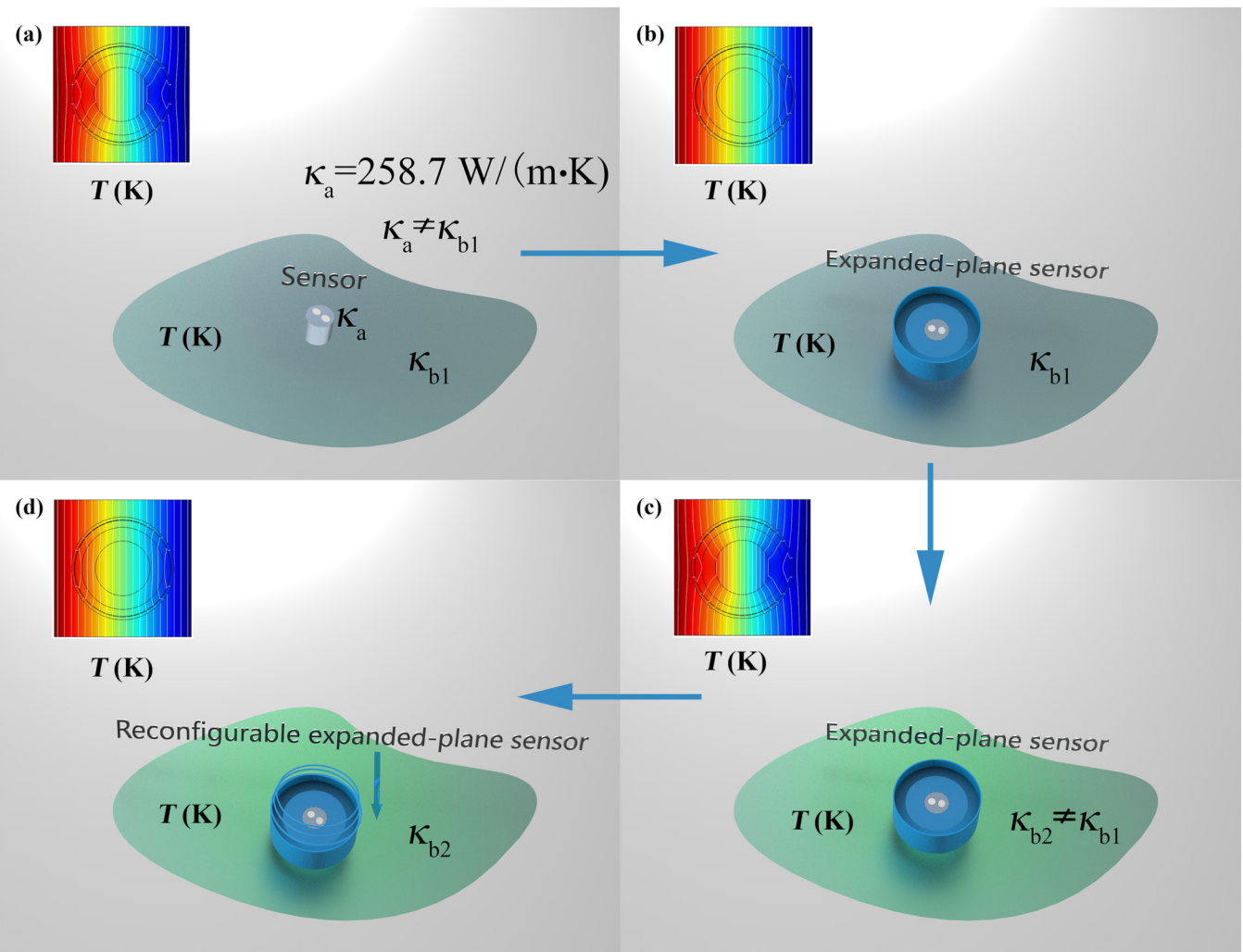


**FIG. 1.** The figure illustrates (a) a conventional sensor with a distorted temperature field in the background region ( $\kappa_a \neq \kappa_{b1}$ ), (b) the expanded-plane sensor, which effectively eliminates the temperature distortions in the background region, and (c) and (d) the reconfigurable expanded-plane sensor's ability to maintain functionality even as the thermal conductivity of the background region changes from  $\kappa_{b1}$  to  $\kappa_{b2}$  by adjusting the height of the expanded plane.

temperature differences between hot and cold sources. This adaptability is realized through the addition or removal of copper rings on the EP structure. These findings not only broaden the potential applications of thermal sensors but also hold significant implications for the wider field of thermal detection, including industrial applications, environmental monitoring, and medical applications.

## II. PROBLEM STATEMENT

The structure of the SEP bilayer sensor is illustrated in Figs. 2(a1) and (a2), where the substrate's dimensions are represented by  $L$  (length),  $L$  (width), and  $v$  (thickness). The core, inner, and outer shell radii are denoted as  $R_1$ ,  $R_2$ , and  $R_3$ , respectively. Additionally, the height and thickness of the outer expanded plane are specified as  $h_3$  and  $d$ , respectively. Given that the thickness of both the substrate and the expanded plane is considered sufficiently small, vertical (along the  $z$  direction) temperature variations on the substrate can be disregarded, and the temperature profile on the expanded plane only changes along the  $z$  direction.<sup>36</sup> In order to achieve the desired sensor effect, it is crucial for the temperature profile in the background region to remain undistorted, with an equal temperature gradient between the core and the background region. This is accomplished by solving the steady-state diffusion equation<sup>45–47</sup>, and the resulting temperature distribution for each region can be expressed as follows:<sup>17</sup>

$$T_1 = Ar \cos \theta \quad (r < R_1), \quad (1a)$$

$$T_2 = Br \cos \theta + \frac{C \cos \theta}{r} \quad (R_1 < r < R_2), \quad (1b)$$

$$T_3 = Dr \cos \theta + \frac{E \cos \theta}{r} \quad (R_2 < r < R_3), \quad (1c)$$

$$T_4 = Ar \cos \theta \quad (r > R_3), \quad (1d)$$

where  $T_1$ ,  $T_2$ ,  $T_3$ , and  $T_4$  represent the temperature distribution of the core, inner shell, outer shell, and background region, respectively. The constants  $A$ ,  $B$ ,  $C$ ,  $D$ , and  $E$  depend on the boundary conditions. The distance between the field point and the origin is denoted by  $r$ , and  $\theta$  represents the polar angle, as shown in Fig. 2(a3). We assume that the expanded plane's boundaries are adiabatic, except for the bottom boundary. Since the temperature is continuous at the boundary between the expanded plane and the substrate, we can obtain the temperature distribution on the expanded plane,  $T_5$ , as follows:<sup>36</sup>

$$T_5 = \frac{AR_3 \cos \theta}{\cosh\left(\frac{h_3}{R_3}\right)} \cosh\left(\frac{h_3 - z}{R_3}\right). \quad (2)$$

Further considering the boundary conditions of temperature consistency and flux continuity between two adjacent regions, we can obtain the following system of equations:

$$AR_3 = DR_3 + \frac{E}{R_3}, \quad (3a)$$

$$\kappa_4 A = \kappa_5 A \tanh\left(\frac{h_3}{R_3}\right) + \kappa_3 \left(D - \frac{E}{R_3^2}\right), \quad (3b)$$

$$DR_2 + \frac{E}{R_2} = BR_2 + \frac{C}{R_2}, \quad (3c)$$

$$\kappa_3 \left(D - \frac{E}{R_2^2}\right) = \kappa_2 \left(B - \frac{C}{R_2^2}\right), \quad (3d)$$

$$BR_1 + \frac{C}{R_1} = AR_1, \quad (3e)$$

$$\kappa_2 \left(B - \frac{C}{R_1^2}\right) = \kappa_1 A, \quad (3f)$$

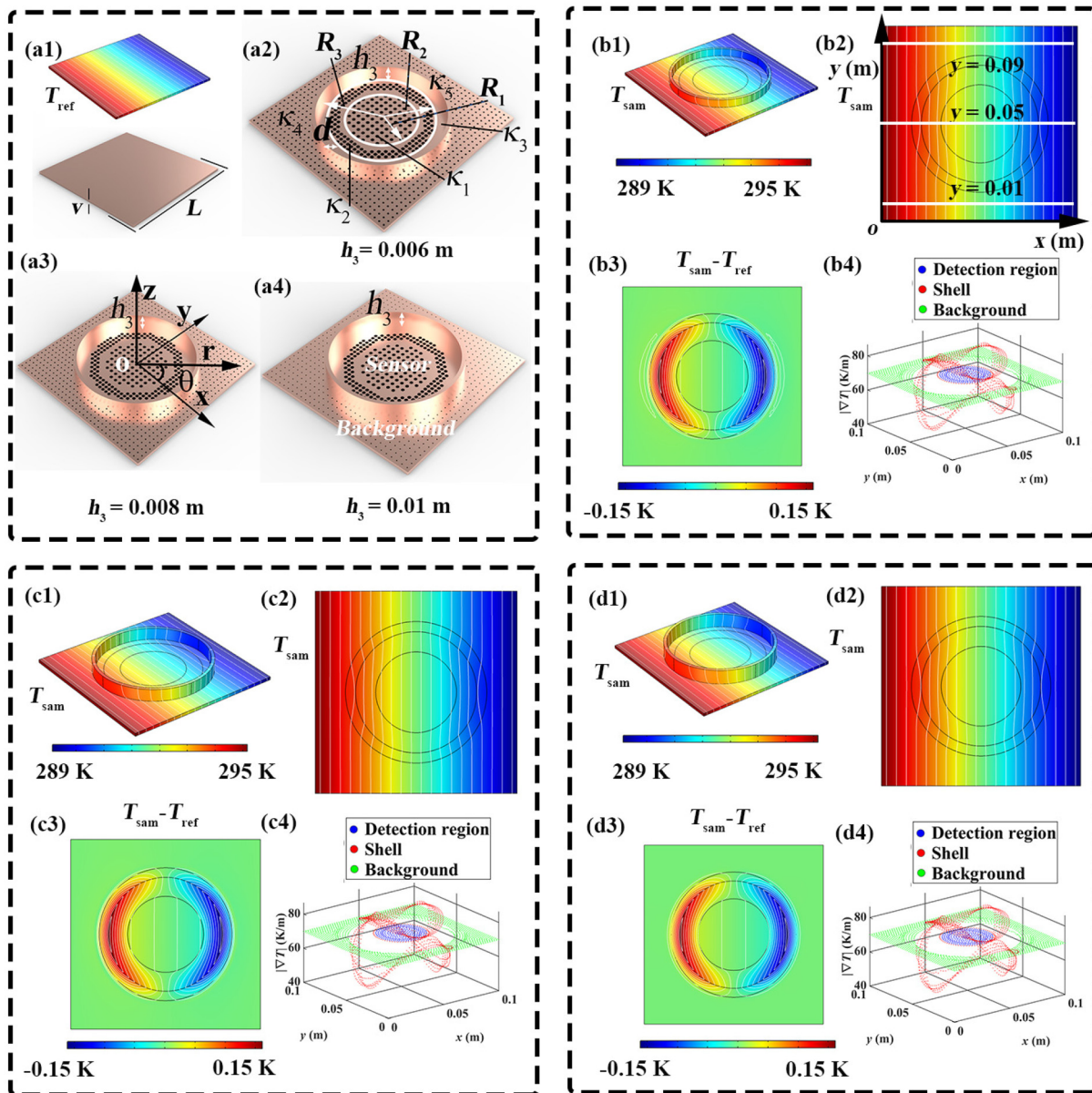
where  $\kappa_1$ ,  $\kappa_2$ ,  $\kappa_3$ ,  $\kappa_4$ , and  $\kappa_5$  represent the thermal conductivity of the core, inner shell, outer shell, background region, and expanded plane, respectively. Using Eqs. (3a)–(3f), we consider  $B$ ,  $C$ ,  $D$ ,  $E$ ,  $h_3$ , and  $\kappa_3$  as the six variables, while other parameters are regarded as coefficients. We can obtain the expression of  $h_3$  as a function of  $R_1$ ,  $R_2$ ,  $R_3$ ,  $\kappa_1$ ,  $\kappa_2$ ,  $\kappa_4$ , and  $\kappa_5$  (see the Appendix).

## III. FINITE-ELEMENT SIMULATIONS

To validate the theoretical analysis presented above, we conducted finite-element simulations using COMSOL MULTIPHYSICS (<https://cn.comsol.com/>). Indeed, for solving the heat transfer problem, there are several alternative methods available, such as the Legendre wavelet collocation method,<sup>41,43</sup> a hybrid numerical method based on Taylor-Galerkin and Legendre wavelets,<sup>42</sup> and the heat-balance integral method.<sup>44</sup> However, considering the advantages offered by the finite-element method, including geometry flexibility, mesh refinement capabilities, and its wide range of applications in the physical sciences, we chose it as our method of verification.

The simulation parameters were configured as follows:  $L = 0.1$  m,  $R_1 = 0.02$  m,  $R_2 = 0.03$  m,  $R_3 = 0.035$  m,  $\kappa_1 = 258.7$  W/(m K),  $\kappa_2 = 213.5$  W/(m K),  $\kappa_3 = 400$  W/(m K), and  $\kappa_5 = 400$  W/(m K). Three different values of  $\kappa_4$  were selected:  $\kappa_4 = 338.7$  W/(m K),  $\kappa_4 = 359.6$  W/(m K), and  $\kappa_4 = 379.9$  W/(m K), each corresponding to different values of  $h_3$  as follows:  $h_3 = 0.006$ , 0.008, and 0.01 m. It should be noticed that the values of  $\kappa_1$ ,  $\kappa_2$ , and  $\kappa_4$  are not set at random but for fabricating convenience of experimental samples (see the Experiments section).

The simulation results for  $h_3 = 0.006$  m are depicted in Figs. 2(b1)–(b4). We have plotted the temperature difference between the sample and reference in Fig. 2(b3). Additionally, the temperature gradient in the core region matches that in the background, which is further emphasized by the temperature gradient distribution on the bottom surface, as illustrated in Fig. 2(b4). In addition, we plot the temperature distributions of three lines on the bottom surface of our structures, i.e.,  $y = 0.01$ , 0.05, and 0.09 m, as is shown in Fig. 3(a). These results provide a vivid visualization of the sensor effect.



03 June 2024 10:32:02

**FIG. 2.** (a1) The structure of the reference and its temperature distribution are depicted. The simulation employs the following parameters:  $L = 0.1 \text{ m}$ ,  $R_1 = 0.02 \text{ m}$ ,  $R_2 = 0.03 \text{ m}$ ,  $R_3 = 0.035 \text{ m}$ ,  $v = 0.002 \text{ m}$ ,  $d = 0.002 \text{ m}$ ,  $\kappa_1 = 258.7 \text{ W/(m K)}$ ,  $\kappa_2 = 213.5 \text{ W/(m K)}$ ,  $\kappa_3 = 400 \text{ W/(m K)}$ , and  $\kappa_5 = 400 \text{ W/(m K)}$ . The thermal conductivity of the background region is as follows: (a2)  $\kappa_4 = 338.7 \text{ W/(m K)}$ ; (a3)  $\kappa_4 = 359.6 \text{ W/(m K)}$ ; (a4)  $\kappa_4 = 379.9 \text{ W/(m K)}$ . The corresponding height of expanded plane is  $h_3 = 0.006$ ,  $0.008$ , and  $0.01 \text{ m}$ , respectively. (b1)–(b4) The simulation presents the temperature distribution, the temperature difference between structure in (a2) and the reference, and the temperature gradient for structure in (a2). (c1)–(c4) The corresponding simulation results are shown for the structure in (a3). (d1)–(d4) The corresponding simulation results are shown for the structure in (a4).

Furthermore, corresponding simulation results for  $h_3 = 0.008$  and  $0.01 \text{ m}$  are presented in Figs. 2(c1)–(c4) and 2(d1)–(d4), respectively. Combined with the results in Figs. 3(b) and 3(c), we see that the temperature distribution of the background region

remains undistorted while the temperature gradient of the core region is the same as that of the background region. This proves the excellent performance of the designed thermal sensor when operating in different background conditions.

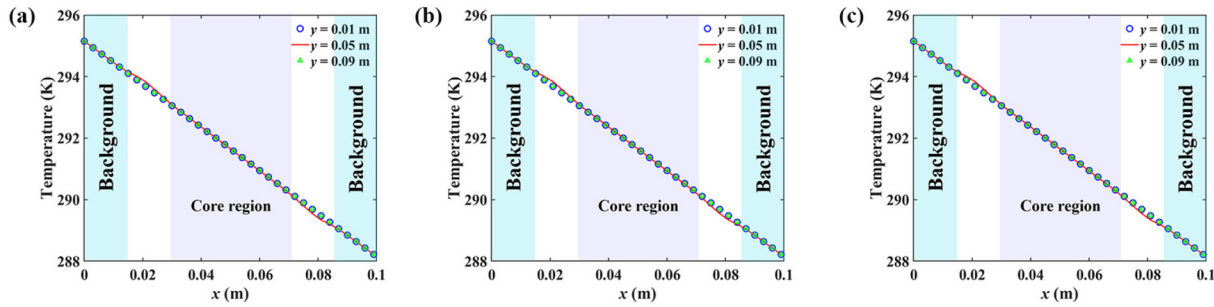
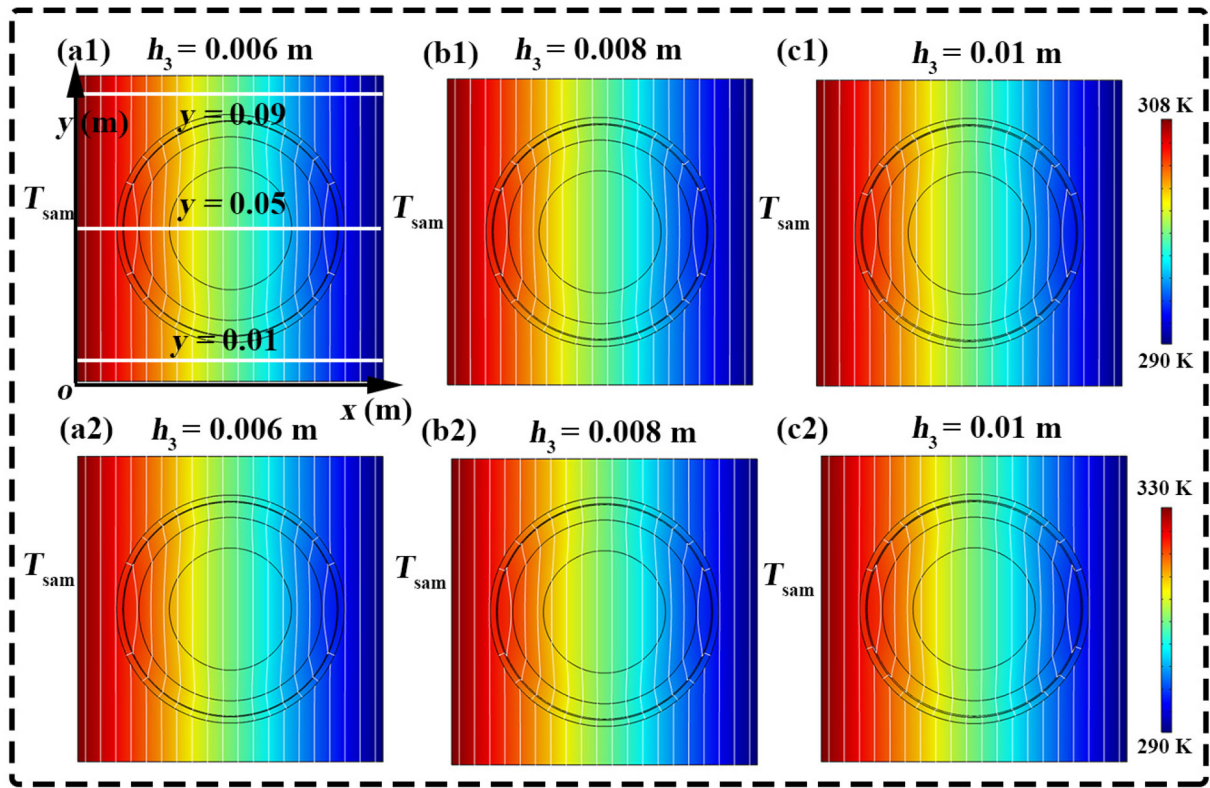


**FIG. 3.** (a)–(c) The temperature distribution of three lines on the bottom surface, i.e.,  $y = 0.01, 0.05, 0.09 \text{ m}$  of structures in Figs. 2(b2), (c2), and (d2).

To demonstrate the versatility of our design in accommodating various temperature fields, we adjusted the temperature difference between the linear heat sources. The simulation results confirm that our structure remains functional even when the temperature difference is altered [see Figs. 4(a1)–(c2) and 5(a)–5(f)].

#### IV. THEORY EXTENSION TO THE MULTIPLE EXPANDED-PLANES CASE

To extend the theoretical analysis presented above the MEP case, we consider another expanded plane with a height of  $h_1$  located in the core region [see Fig. 6(a2)]. The thickness of this plane can also be ignored. Then, the temperature distribution of



03 June 2024 10:32:02

**FIG. 4.** (a1), (a2), (b1), (b2), (c1), and (c2) The corresponding simulation results are presented for the structure in Figs. 2(a2)–(a4) with the temperature difference being 20 and 35 K, respectively.

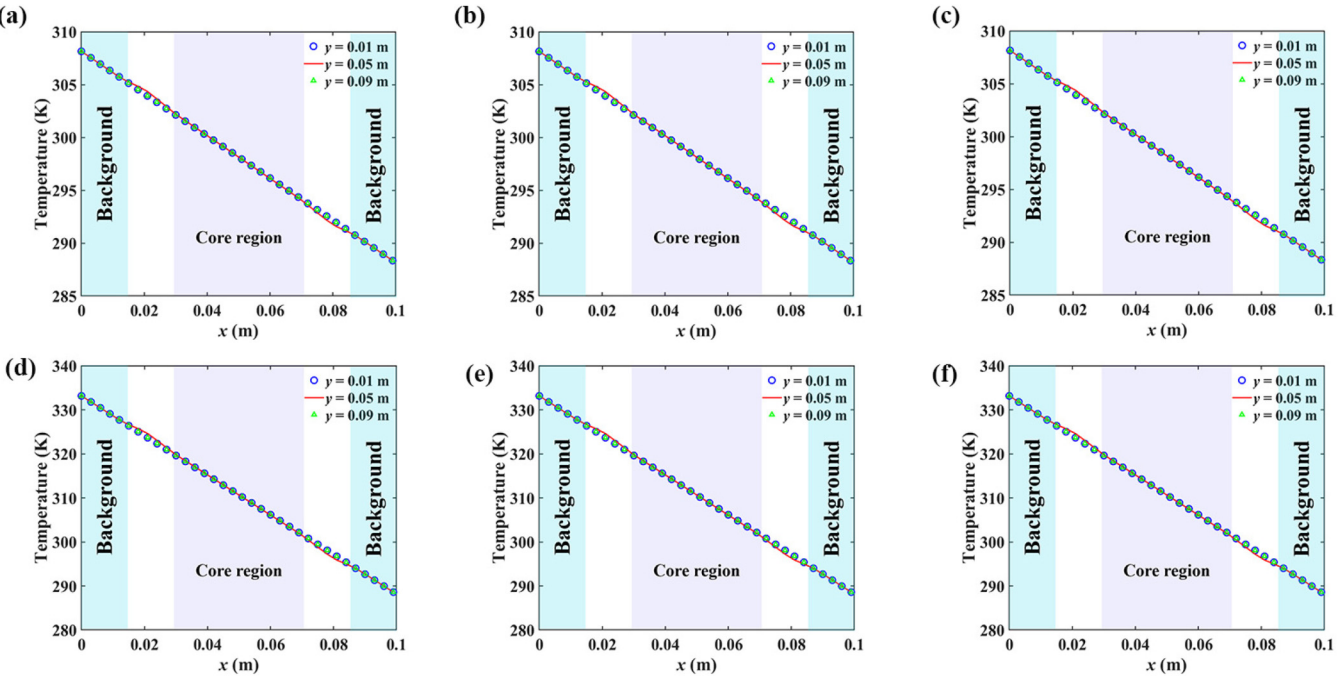


FIG. 5. (a)–(f) The corresponding temperature distribution of three lines on the bottom surface, i.e.,  $y = 0.01, 0.05, 0.09$  m of structures in Figs. 4(a1), (b1), (c1), (a2), (b2), and (c2).

03 June 2024 10:32:02

the core expanded plane  $T_6$  can be expressed as follows:

$$T_6 = \frac{AR_1 \cos \theta}{\cosh\left(\frac{h_1}{R_1}\right)} \cosh\left(\frac{h_1 - z}{R_1}\right). \quad (4)$$

Accordingly, we replace Eq. (3f) by

$$\kappa_2 \left( B - \frac{C}{R_1^2} \right) = \kappa_1 A + \kappa_6 F \tanh\left(\frac{h_1}{R_1}\right), \quad (5)$$

where  $\kappa_6$  represents the thermal conductivity of the inner expanded plane. In this case, we consider  $B$ ,  $C$ ,  $D$ ,  $E$ ,  $h_1$ , and  $h_3$  as variables. By following a similar approach as before, we can obtain an expression for  $h_1$  and  $h_3$  as a function of the other parameters (see the Appendix). It should be noted that a significant advantage of the MEP sensor is its capability to adapt to the thermal conductivity of the core region. The expressions for  $h_1$  and  $h_3$  illustrate that while  $h_1$  is dependent on  $\kappa_1$ ,  $h_3$  is not influenced by it. This indicates that the MEP structure can accommodate core regions with varying thermal conductivities by merely adjusting the value of  $h_1$ .

## V. FINITE-ELEMENT SIMULATIONS FOR THE MULTIPLE EXPANDED-PLANES CASE

In the MEP case, the values of  $L$ ,  $R_1$ ,  $R_2$ ,  $R_3$ ,  $\kappa_3$ , and  $\kappa_5$  are set to the same values as in the SEP case. The values of  $h_1$  and  $\kappa_6$  are set as follows:  $h_1 = 6.5$  mm,  $\kappa_6 = 400$  W/(m K). Certain parameters

are changed as the following values:  $\kappa_1 = 190.0$  W/(m K),  $\kappa_2 = 280.0$  W/(m K). To implement the thermal sensor, three sets of values are chosen for  $\kappa_4$ :  $\kappa_4 = 340.0, 360.0, 380.0$  W/(m K). The corresponding values for  $h_3$  are as follows:  $h_3 = 1.7, 3.5, 5.2$  mm. Similar to the SEP case, the temperature distribution, temperature difference between the sample and the reference, and temperature gradient on the bottom surface are presented for the three cases [see Figs. 6(b1)–(d4)]. The more quantitative results are shown in Figs. 7(a)–7(c). For the MEP cases, the temperature distribution of the background region also remains undistorted while the temperature gradient of the core region is the same as that of the background region. These results demonstrate that the MEP structure ensures the excellent performance of a dynamic thermal sensor.

## VI. EXPERIMENTS

To validate the theory of the reconfigurable expanded-plane thermal sensor, we conducted experiments in the context of the SEP case. Three copper samples were chosen due to their high thermal conductivity,<sup>48,49</sup> as illustrated in Figs. 8(d1)–(d3). The parameters for the first sample were defined as follows:  $L = 0.1$  m,  $R_1 = 0.02$  m,  $R_2 = 0.03$  m,  $R_3 = 0.035$  m,  $h_3 = 0.006$  m,  $\kappa_1 = 258.7$  W/(m K),  $\kappa_2 = 213.5$  W/(m K),  $\kappa_3 = 400$  W/(m K),  $\kappa_4 = 338.7$  W/(m K), and  $\kappa_5 = 400$  W/(m K). These parameters are consistent with those depicted in Fig. 2(b1). To achieve the desired thermal conductivity for each region, we employed a specific number of holes following the principles of the effective

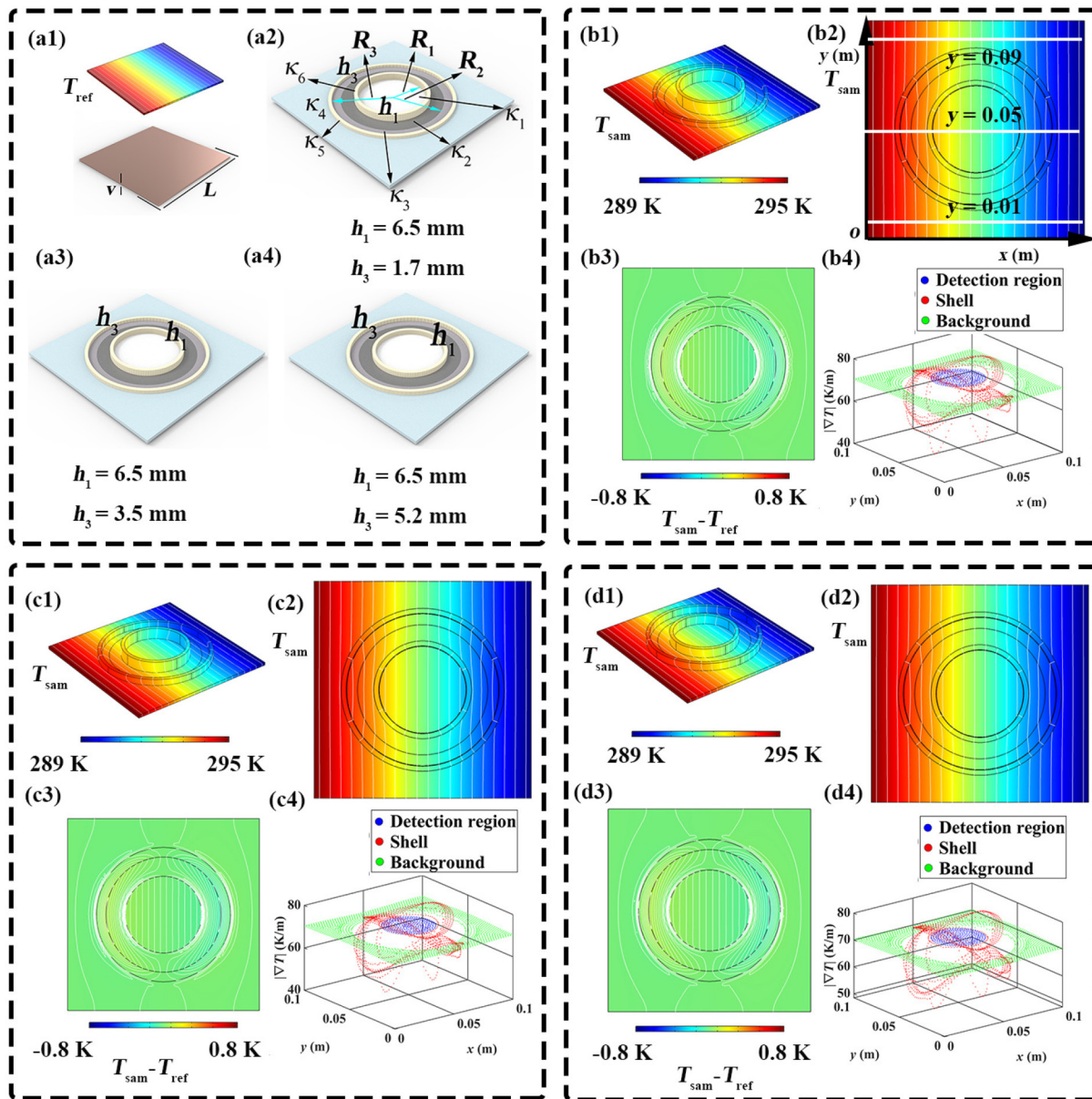


**FIG. 6.** (a1) The figure illustrates the structure of the reference and its corresponding temperature distribution. Additionally, (a2)–(a4) present the structures of the MEP bilayer sensor with varying heights for the inner and outer expanded planes. The simulation employs the following parameters:  $L = 0.1\text{ m}$ ,  $R_1 = 0.02\text{ m}$ ,  $R_2 = 0.03\text{ m}$ ,  $R_3 = 0.035\text{ m}$ ,  $v = 0.002\text{ m}$ ,  $d = 0.002\text{ m}$ ,  $\kappa_1 = 190\text{ W/(m K)}$ ,  $\kappa_2 = 280\text{ W/(m K)}$ ,  $\kappa_3 = 400\text{ W/(m K)}$ ,  $\kappa_5 = 400\text{ W/(m K)}$ ,  $\kappa_6 = 400\text{ W/(m K)}$ , and  $h_1 = 6.5\text{ mm}$ . The specific values for thermal conductivity of the background region are as follows: (a2)  $\kappa_4 = 340.0\text{ W/(m K)}$ ; (a3)  $\kappa_4 = 360.0\text{ W/(m K)}$ ; (a4)  $\kappa_4 = 380.0\text{ W/(m K)}$ . The corresponding height of the outer expanded plane is  $h_3 = 1.7, 3.5$ , and  $5.2\text{ mm}$ , respectively. (b1)–(b4) The simulation results depict the temperature distribution, the temperature difference between the structure in (a2) and the reference, and the temperature gradient for the structure in (a2). (c1)–(c4) The corresponding simulation results are presented for the structure in (a3). (d1)–(d4) The corresponding simulation results are presented for the structure in (a4).

medium theory.<sup>50–52</sup> Assuming thermal conductivity values of  $400\text{ W/(m K)}$  for copper and  $0.03\text{ W/(m K)}$  for air, we determined area fractions of 21.5%, 30.4%, and 8.3% for the core, inner shell, and background regions, respectively. The hole diameters were set

at 2, 1, and  $0.6\text{ mm}$ , requiring drilling of 86, 152, and 602 holes, respectively. This same methodology was applied to the second and third samples, with their parameters matching those of the simulated samples shown in Figs. 2(c1) and (d1).

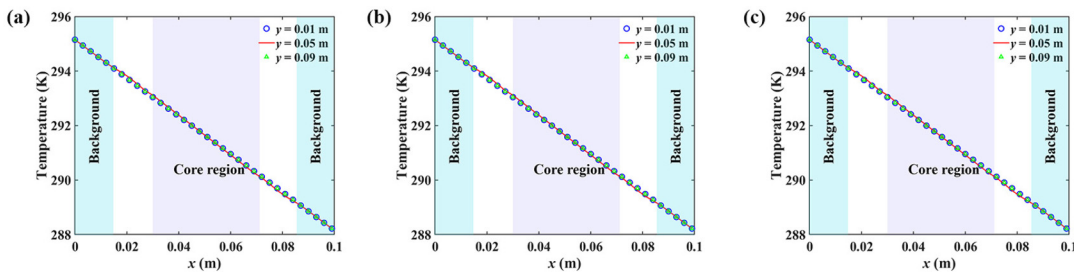
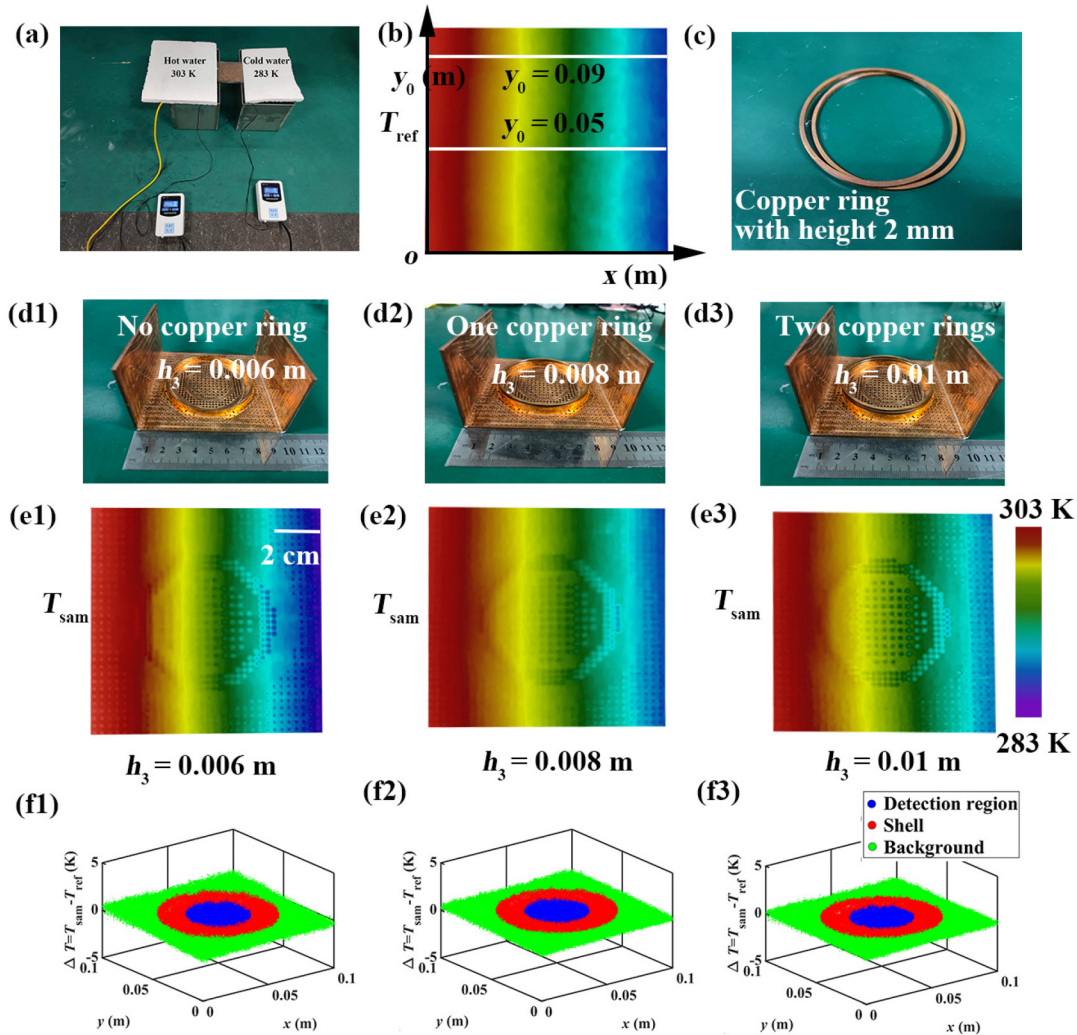
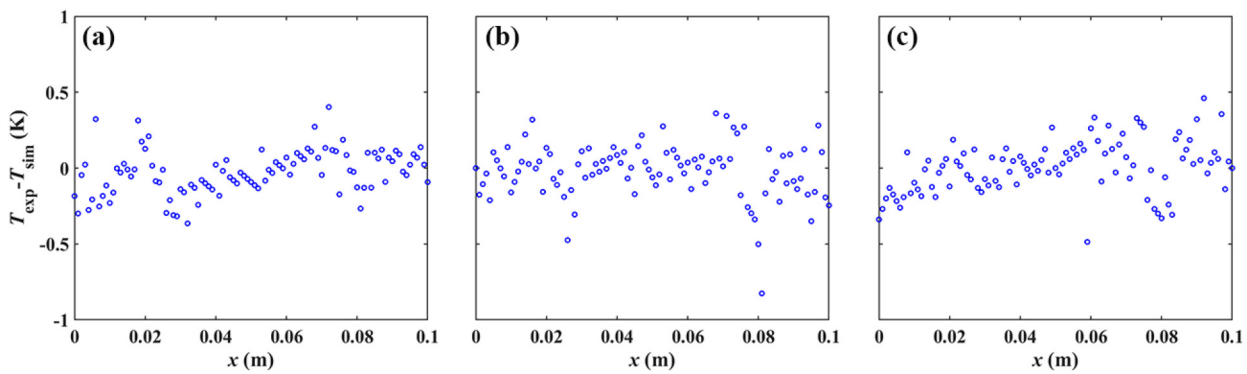


FIG. 7. (a)–(c) The corresponding temperature distribution of three lines on the bottom surface, i.e.,  $y = 0.01, 0.05, 0.09 \text{ m}$  of structures in Figs. 6(b2), (c2), and (d2).



03 June 2024 10:32:02

FIG. 8. (a) The experimental setup is described. (b) The experimental results for the reference are presented. (c) Copper rings with a height of 2 mm are utilized. (d1)–(d3) The structures of three samples are illustrated. (e1)–(e3) The experimental results for the three samples are shown. (f1)–(f3) The temperature difference between the samples and the reference is analyzed.



**FIG. 9.** (a)–(c) The difference between experimental  $T_{\text{exp}}$  and simulation  $T_{\text{sim}}$  results along the central line, i.e.,  $y = 0.05 \text{ m}$  for three cases, corresponding to Fig. 2(b2) and Fig. 8(e1); Fig. 2(c2) and Fig. 8(e2); Fig. 2(d2) and Fig. 8(e3), respectively. The temperature periods of the experimental results have been adjusted to match those of the simulation results.

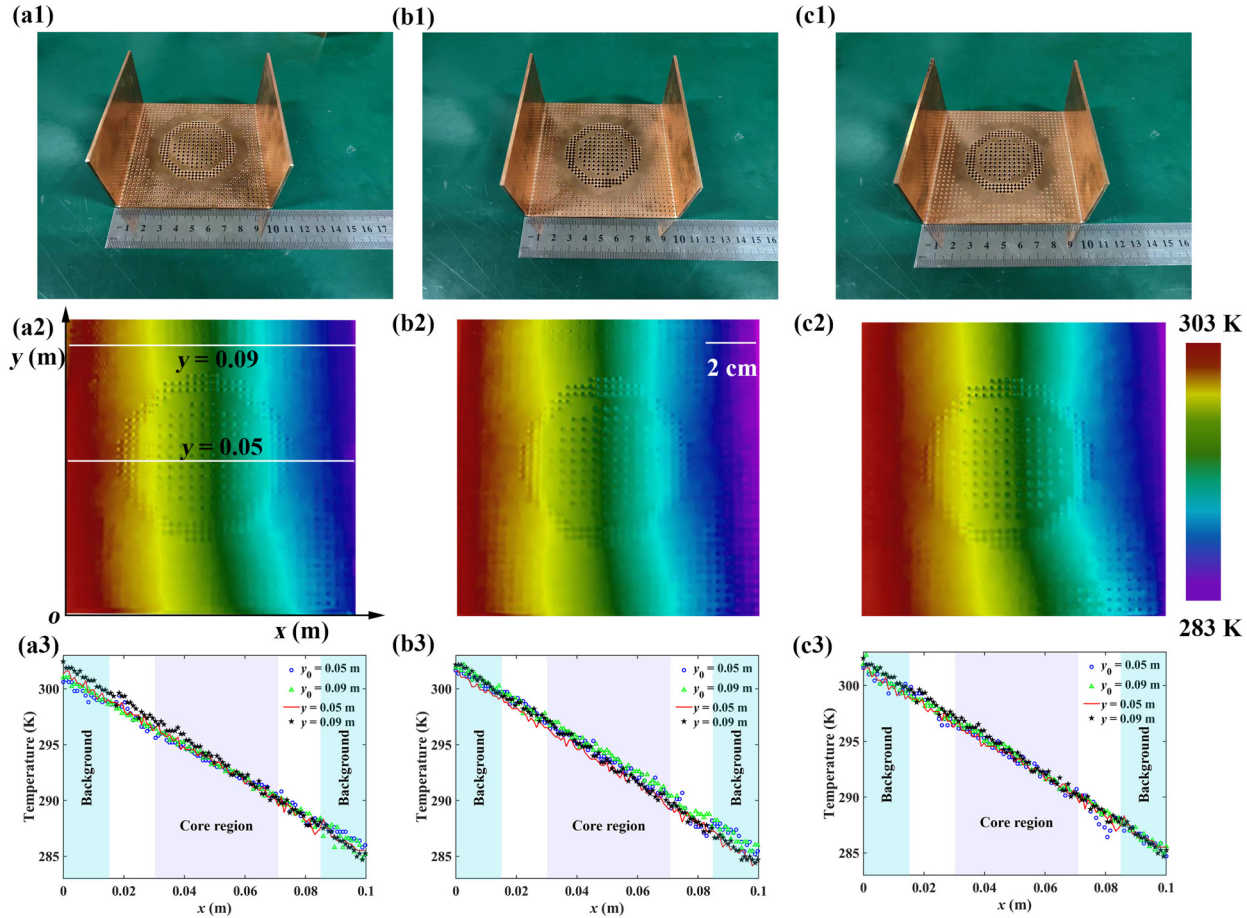


**FIG. 10.** (a1)–(c1) The corresponding reference sample of Figs. 2(a2)–(a4) without expanded plane. (a2)–(c2) The corresponding experimental results for (a1)–(c1). (a3)–(c3) The temperature distributions of two lines for structures in (a2)–(c2), i.e.,  $y = 0.05, 0.09 \text{ m}$ , and in Fig. 8(b), i.e.,  $y_0 = 0.05, 0.09 \text{ m}$ .

03 June 2024 10:32:02

To realize the reconfigurable expanded-plane sensor, we prepared a series of copper rings each with a height of 2 mm [Fig. 8(c)] and adjusted the height of the expanded plane by adding or removing these rings. To compensate for changes in the thermal conductivity of the background region (in the case of the second and third samples), one ring and two rings were added to the expanded plane, respectively. We filled thermal grease between the rings, allowing us to consider the thermal resistance of the expanded plane as negligible. Furthermore, as illustrated in Figs. 8(e1)–(e3), the experimental outcomes demonstrate enhanced thermal sensing performance. This observation corroborates the premise that the impact of the current thermal contact resistance (TCR) is insignificant. Although the TCR between each layer of our sample (core region, inner shell, outer shell, and background) is considered zero, TCR inevitably exists in our designed structure when applied in real-world settings due to the differing materials of each layer. This variance significantly impacts the sensor effect of our design. Notably, our theoretical framework assumes continuity in temperature between each layer, thereby overlooking the TCR. However, considering the influence of TCR, our theory necessitates modifications, as there will be a temperature discontinuity at each interface. Li *et al.* have explored interfacial thermal resistance from a microscopic perspective.<sup>53</sup> Similarly, other studies have addressed related topics.<sup>54</sup> Given that TCR is influenced by the size of the materials, it is imperative to minimize the size of our design when implementing it in practical applications.

The experimental setup is depicted in Fig. 8(a). One side of the sample was brought into contact with a hot source at a temperature of 303 K, while the other side was connected to a cold source at 283 K. Once the system reached a stable state, an infrared camera was employed to capture the surface of the sample from the top and record the temperature distribution. The resulting temperature distributions of the sample surfaces are presented in Figs. 8(e1)–(e3) for the three different samples. Additionally, the experimental result of the reference is shown in Fig. 8(b). To illustrate the thermal sensor effect, on the one hand, we present the temperature difference between the sample and the reference, as demonstrated in Figs. 8(f1)–(f3). We see that the temperature difference primarily resides within the plane where  $\Delta T = 0$ . These findings validate the exceptional performance of the samples and substantiate the accuracy of our thermal sensor theory. Additionally, we utilize the simulation results as a benchmark to gauge the accuracy of our experimental outcomes. For the three samples, we present the temperature differences between the experimental and corresponding simulation results along the central line, i.e.,  $y = 0.05$  m, as illustrated in Figs. 9(a)–9(c). We note that the temperature difference is approximately zero along  $y = 0.05$  m for our three structures. This observation further confirms the precision of the experimental results.

Furthermore, we conducted experiments for the reference sample without an expanded plane [see Figs. 10(a1)–(a3)]. In this case, the thermal conductivity of each region matched that of the corresponding EP structure. To show that the structures without EP planes cannot achieve the desired sensor effect, we plot the temperature distributions of two lines on the bottom surface of each structure, i.e.,  $y = 0.05, 0.09$  m. We also compare the results with that of the reference [see Figs. 10(a3)–(c3)]. The experimental

results revealed temperature field distortion for structures lacking an expanded plane [see Figs. 10(a2)–(a3)]. This further proves the effectiveness of our EP design.

## VII. DISCUSSION AND CONCLUSION

Expanding upon the single expanded-plane structure, we have successfully engineered a reconfigurable sensor. Our simulation and experimental results provide robust evidence of the device's ability to operate effectively across a wide range of background environments, achieved simply by adjusting the height of the expanded plane. Furthermore, we have extended our investigations to scenarios involving multiple expanded planes, and we have obtained consistent and reliable results. In comparison to the conventional two-dimensional sensor structure, the expanded plane is an integral component of the proposed design. Nonetheless, we define the core region delineated by the radius  $R_1$  as the operational area of the sensor, and the background region as the area external to the circle represented by the radius  $R_3$ , as depicted in Figs. 2(a2)–(a4). To achieve the desired sensor effect, it is crucial to ensure that the thermal conductivity of each region matches appropriately.<sup>31</sup> According to conventional two-dimensional sensor theory, the thermal conductivity of the outer layer region should significantly exceed that of the background region. Although the thermal conductivity of the outer layer region for the expanded-plane structure is only 400 W/(m K), the effective thermal conductivity of the outer layer can reach an ultrahigh value since a portion of the heat flux is directed toward the expanded plane. This is why we can ensure that the temperature distribution remains undistorted using the EP (expanded-plane) structure. It should be noted that to address the issue of distortion, employing a non-contact measurement method such as an infrared camera offers a viable alternative.<sup>55</sup> As a non-contact approach, it allows for temperature measurement without the necessity of physical contact with the object, thereby preserving the integrity of the original temperature field. However, infrared cameras can only detect thermal radiation from surfaces within their line of sight. If an object is obscured or positioned behind a barrier, effective measurement is not possible. Moreover, different materials exhibit varying emissivities, which can impact the accuracy of measurements. Accurate temperature assessment using an infrared camera necessitates knowledge or estimation of the surface emissivities. Therefore, under such circumstances, our designed structure proves to be more applicable.

However, it is important to note that in this study, we have exclusively focused on the thermal conduction mechanism.<sup>56–58</sup> It is imperative to acknowledge that the influences of thermal radiation<sup>59–61</sup> and convection mechanisms<sup>62</sup> should be considered for further investigation. To enhance the precision of our theoretical framework, it would be advisable to incorporate these variables into future research endeavors. We also recommend that the materials for each layer of our structure should possess low thermal capacity if implemented in practical applications, considering that the temporal response of the sensor is a critical factor. A shorter temporal response time generally indicates higher sensor quality. Therefore, thermal sensors are typically constructed from materials with low thermal capacity.<sup>63</sup> For instance, thermocouples are made from metals such as copper, nickel, and chromium. The temporal





- <sup>54</sup>J. Chen, X. Xu, J. Zhou, and B. Li, "Interfacial thermal resistance: Past, present, and future," *Rev. Mod. Phys.* **94**, 025002 (2022).
- <sup>55</sup>T. Onaka, H. Matsuhara, T. Wada, N. Fujishiro, H. Fujiwara, M. Ishigaki, D. Ishihara, Y. Ita, H. Kataza, W. Kim *et al.*, "The infrared camera (IRC) for AKARI—Design and imaging performance," *Publ. Astron. Soc. Jpn.* **59**, S401–S410 (2007).
- <sup>56</sup>L. Xu, J. Liu, P. Jin, G. Xu, J. Li, X. Ouyang, Y. Li, C.-W. Qiu, and J. Huang, "Black-hole-inspired thermal trapping with graded heat-conduction metadevices," *Nat. Sci. Rev.* **10**, nwac159 (2023).
- <sup>57</sup>H. Tan, Y. Qiu, L. Xu, and J. Huang, "Tunable thermal conduction force without macroscopic temperature gradients," *Phys. Rev. E* **108**, 034105 (2023).
- <sup>58</sup>J. He, C. Yu, S. Lu, Z. Zhang, and J. Chen, "Importance of hydrogen bond configuration on lattice thermal conductivity of hydrogenated borophene," *Appl. Phys. Lett.* **124**, 022201 (2024).
- <sup>59</sup>B. Xie, Y. Liu, W. Xi, and R. Hu, "Colored radiative cooling: Progress and prospects," *Mater. Today Energy* **34**, 101302 (2023).
- <sup>60</sup>M. Powalla, S. Paetel, E. Ahlsweide, R. Wuerz, C. D. Wessendorf, and T. Magorian Friedlmeier, "Thin-film solar cells exceeding 22% solar cell efficiency: An overview on CdTe-, Cu (In, Ga) Se<sub>2</sub>-, and perovskite-based materials," *Appl. Phys. Rev.* **5**, 041602 (2018).
- <sup>61</sup>M. Wiesenfarth, I. Anton, and A. W. Bett, "Challenges in the design of concentrator photovoltaic (CPV) modules to achieve highest efficiencies," *Appl. Phys. Rev.* **5**, 041601 (2018).
- <sup>62</sup>R. Ju, P.-C. Cao, D. Wang, M. Qi, L. Xu, S. Yang, C.-W. Qiu, H. Chen, and Y. Li, "Nonreciprocal heat circulation metadevices," *Adv. Mater.* **36**, 2309835 (2024).
- <sup>63</sup>W. Chickering, J. Eisenstein, and J. Reno, "Hot-electron thermocouple and the diffusion thermopower of two-dimensional electrons in GaAs," *Phys. Rev. Lett.* **103**, 046807 (2009).
- <sup>64</sup>T. Yang, X. Bai, D. Gao, L. Wu, B. Li, J. T. Thong, and C.-W. Qiu, "Invisible sensors: Simultaneous sensing and camouflaging in multiphysical fields," *Adv. Mater.* **27**, 7752–7758 (2015).
- <sup>65</sup>M. Lei, J. Wang, G. Dai, P. Tan, and J. Huang, "Temperature-dependent transformation multiphysics and ambient-adaptive multiphysical metamaterials," *Europhys. Lett.* **135**, 54003 (2021).
- <sup>66</sup>M. Lei, L. Xu, and J. Huang, "Spatiotemporal multiphysics metamaterials with continuously adjustable functions," *Mater. Today Phys.* **34**, 101057 (2023).
- <sup>67</sup>P. Zhuang and J. Huang, "Multiple control of thermoelectric dual-function metamaterials," *Int. J. Mech. Syst. Dyn.* **3**, 127–135 (2023).
- <sup>68</sup>F. Sun, J. Zhu, and D. Tang, "Thermal conductivity measurement of liquids using femto-second laser pump-probe technique," *Chin. Sci. Bull.* **60**, 1320–1327 (2015).
- <sup>69</sup>C. Bing-Yang and Z. Zi-Tong, "Thermal smart materials and their applications in space thermal control system," *Acta Phys. Sin.* **71**, 014401 (2022).
- <sup>70</sup>R. Hu, S. Huang, M. Wang, L. Zhou, X. Peng, and X. Luo, "Binary thermal encoding by energy shielding and harvesting units," *Phys. Rev. Appl.* **10**, 054032 (2018).
- <sup>71</sup>F. Yang, P. Jin, M. Lei, G. Dai, J. Wang, and J. Huang, "Space-time thermal binary coding by a spatiotemporally modulated metashell," *Phys. Rev. Appl.* **19**, 054096 (2023).